

Emergence of a Bandgap in Nano-scale Graphite: A Computational and Experimental Study

Sujinda Chaiyachad¹, Trung-Phuc Vo^{2,3}, Sirisak Singesen¹, Tanachat Eknapakul^{1,4},
Warakorn Jindata¹, Chutchawan Jaisuk¹, Patrick Le Fevre⁵, Francois Bertran⁵,
Donghui Lu⁶, Yaobo Huang⁷, Hideki Nakajima⁸, Watchara Liewrian⁹, Ittipon
Fongkaew¹, Ján Minár^{2,*} and Worawat Meevasana^{1,*}

¹School of Physics and Center of Excellence on Advanced Functional Materials,
Suranaree University of Technology, Nakhon Ratchasima 30000, Thailand

²New Technologies-Research Center, University of West Bohemia, 30100, Pilsen,
Czech Republic

³Institute of Physics, Czech Academy of Sciences, Cukrovarnická 10, 16200 Praha 6,
Czech Republic

⁴Functional Materials and Nanotechnology Center of Excellence, School of Science,
Walailak University, Nakhon Si Thammarat, 80160, Thailand

⁵Synchrotron SOLEIL, L'Orme des Merisiers, Départementale 128, F-91190 Saint-
Aubin, France

⁶Stanford Synchrotron Radiation Lightsource, SLAC National Accelerator
Laboratory, 2575 Sand Hill Road, Menlo Park, California 94025, USA

⁷Shanghai Advanced Research Institute, Chinese Academy of Sciences No.99 Haike
Road, Zhangjiang Hi-Tech Park, Pudong Shanghai, P R China

⁸Synchrotron Light Research Institute, Nakhon Ratchasima 30000, Thailand

⁹Department of Physics, King Mongkut's University of Technology Thonburi,
Bangkok 10140, Thailand

E-mail: jminar@ntc.zcu.cz and worawat@g.sut.ac.th

Abstract

Bandgaps in layered materials are critical for enabling functionalities such as tunable photodetection, efficient energy conversion, and nonlinear optical responses, which are essential for next-generation photonic and quantum devices. Gap engineering could form heterostructures with complementary materials like transition metal dichalcogenides or perovskites for multi-functional devices. Graphite, conventionally regarded as a gapless material, exhibits a bandgap of ~ 100 meV in nano-scale patterned highly oriented pyrolytic graphite (HOPG), as revealed by angle-resolved photoemission spectroscopy (ARPES) and Raman measurements. Our state-of-the-art calculations, incorporating photoemission matrix element effects, predict this bandgap with remarkable accuracy and attribute it to mechanical distortions introduced during patterning. This work bridges theory and experiment, providing the direct evidence of a tunable bandgap in HOPG. Beyond its fundamental significance, this finding opens new possibilities for designing materials with tailored electronic properties, enabling advancements in terahertz devices and optoelectronics.

Two-dimensional graphene exhibits remarkable properties with a wide range of applications including high mobility metallic transistor [1] magneto-electronic devices [2] quantum computing devices based on quantum electrodynamics [3] and terahertz (THz) optoelectronics [4,5]. When focusing on the THz devices, THz radiation can pass through media without ionizing and exhibit good chemical sensitivity, enabling applications in security screening, medical imaging and chemical characterizing. Graphene has high potential to be used in THz optoelectronics due to surface plasmonic oscillator which can react effectively with terahertz frequency [6-7]. Unlike TMDs, it responds to visible and near-UV frequencies due to the suitability of the energy gap [8]. Graphene also exhibits the photo-carrier multiplication effect where a single photon can excite more than one electron by Auger process [9]. In photovoltaic devices, carrier multiplication can enhance charge carrier density which can theoretically lead to power conversion efficiency beyond 33% of single-junction devices. However, the light-matter interaction of graphene is still low [10], hindering certain usages. Enhancing the interaction of light and matter in graphene with a high-THz resonance frequency will accelerate the development of THz optoelectronics.

To increase the interaction between light and graphene, the increase in graphene layers can result the light-matter interaction up to 99% in graphite. Graphite plasmonic frequency is in the THz range (~ 34 THz) and its surface plasmon polariton resonant characteristics are close to those of conventional metals [10-12] while narrow bandgap opening in bilayer graphene can further provide high responsivity of THz devices [13]. Moreover, it is known that the light-matter interaction can be enhanced on the array of metasurface with periodic length smaller than light wavelength [14]. Therefore, it is interesting to investigate if nano-scale patterning of multilayer graphene with intrinsic energy gap can further enhance performance of THz optoelectronic devices.

To directly measure the electronic structure, angle-resolved photoemission spectroscopy (ARPES) has been used for observing bandgaps of graphene samples [15-18]. To obtain the band dispersion, the samples need to be single crystals [15-16] but can be small in the forms of graphene islands [17] or multi-grain film [18] (i.e., using nano-ARPES where the beam size is smaller than the samples.) ARPES shows that graphene is a gapless material where its valence band and conduction band intersect at the K point of the Brillouin zone (i.e., Dirac point) [19-21]. There are methods to create intrinsic gap in graphene such as substrate inducing [15] and quantum size effect (graphene quantum dot (GQD) and graphene nano ribbon (GNR) where energy gap depends on its size [22]). Here, by using ARPES measurement, we show the bandgap opening of nano highly oriented pyrolytic graphite (nano-HOPG) which is not observed in pristine HOPG. We further investigated the origin of bandgap opening with Raman spectroscopy and density functional theory (DFT) calculations.

The square nano-scale patterns of HOPG (nano-HOPG) were prepared on a single crystal HOPG substrate (NT-MDT Spectrum Instruments, HOPG YZA Quality, piece size 7x7 mm., thickness 1.8 mm). Their square patterns were created by using the focused ion beam technique (FE-SEM, Zeiss AURIGA), in which a Ga ion was an ion source, with a source voltage of 300 kV and a source current of 100 pA. The 30-nm beam spot size is sputtered on the substrate at a depth of 15 nm. Their electronic structure was measured using ARPES, performed at beamline 09U1 of the Shanghai Synchrotron Radiation Facility, China, using photon energy 95 eV and a Scienta DA30L electron analyzer. Note that the surface of nano-HOPG was cleaned by heating the sample at 500 °C before ARPES measurement. The ARPES measurement was performed immediately after cleaning the surface in an ultra-high vacuum at a pressure better than 4×10^{-11} Torr. The energy resolution was set at 15 meV, and the sample

temperature was maintained at 15 K throughout the experiment. Since the dimension of nano-HOPG pattern is $100 \times 100 \mu\text{m}^2$, the smaller beam spot size of $20 \times 30 \mu\text{m}^2$ was used to measure the areas of HOPG samples covering on and off-grids nano-scale patterns. To locate the nano-scale pattern, we identified the edges of the HOPG substrate as referenced points. Next, we performed ARPES measurements in the $300 \times 300 \mu\text{m}^2$ array with a step size of $100 \mu\text{m}$ in x and y directions (i.e., 3×3 grid). The symmetrized EDCs of band dispersion of the ARPES measurements array is shown in Fig. S1. We also measured the ARPES data at the location far away from the nano-scale pattern at approximately 1 mm to compare and contrast the spectra. In addition, the Raman spectroscopy was used to observe disorder structure at room temperature with a laser wavelength of 532 nm, a beam size of $4 \mu\text{m}$, and a laser power of 50 mW.

To cope with spectroscopic and many-body aspects in ARPES, the Green's function Korringa-Kohn-Rostoker (KKR) method [23] was applied under multiple scattering formalism implemented in the SPRKKR package [24]. As a result, corresponding calculations were carried out within the fully relativistic Dirac formalism and spin density functional theory, taking into account spin-orbit coupling (SOC) impacts. No shape approximations are made for the description of the potential as we use the full potential approach. In addition, the exchange-correlation energy functional was treated by local density approximation (LDA) and the ground state computations were conducted using the observed lattice constant [25] of $a = 2.456 \text{ \AA}$, $b = 2.456 \text{ \AA}$, and $c = 6.696 \text{ \AA}$. The maximum value of the angular momentum quantum number is truncated at $l_{\text{max}} = 3$. Lloyd's formula has been employed for accurate determination of the Fermi level [26]. To achieve convergence in the multiple scattering between layers, our calculations utilized a plane-wave basis, increasing the surface reciprocal lattice vectors \vec{G} to 37. A key parameter in describing multiple scattering involves the

expansion of all physical quantities using l_{\max} , employing Bauer's identity to represent plane waves (interlayer scattering) with spherical waves (intralayer scattering). The final state is represented by a time-reversed LEED (TR-LEED) state from Pendry's model [27-29], allowing the accurate description of these states in a wide range of photon energies (from 6 eV up to several keV) [30-33]. Strocov et al. demonstrated that TR-LEED treatment can disentangle the multiband final states giving rise to the broadening of the ARPES peaks in the Ag metal [34]. For obtaining as close as agreements with experiments, ARPES calculations were conducted based on the one-step model (ISM) of photoemission [35,36]. Consequently, the theory accounts for influences triggered by the light polarization, matrix-element effects and surface effects [37,38]. Recently, ISM simulations were successfully in capturing the typical characteristics of a new type of magnetism, so-called alter-magnetism [39]. This theoretical work provides significant benefits for the emerging field of spintronics, a next-generation magnetic memory technology. The solid surface in the current study is described by semi-infinite lattices with ideal lateral translation invariance and arbitrary number of atoms per unit cell. The computational model described here is applied to the valence band in this work but is also effective for core levels [40-42]. More details regarding the core-level implementation can be found in Ref [43], which elucidates the photoelectron effects responsible for the pronounced modulation of ARPES patterns. To further understand the strain dependence, we use the density functional theory (DFT) calculation as implemented in the VASP code [44-45] to calculate the band dispersion along k_z direction of the 1.1% for biaxial tensile strains. The generalized gradient approximation (GGA) of Perdew-Burke-Ernzerhof (PBE) was used to describe the exchange-correlation functional [46]. The electron-ion interactions were treated by the projector-augmented-wave (PAW) method [47]. Van der Waals correction of the Grimme method

(DFT- D3) has been taken into account to explain long-range interactions [48]. The cutoff energy of 520 eV was set to represent number of plane-wave basis sets. The Monkhorst-pack scheme [49] of $21 \times 21 \times 1$ k-point mesh for Brillouin interaction was used for the calculation of structural optimization and band structure. The structure was fully relaxed until the atomic force acting on each atom was less than 0.01 eV/Å. The band structure calculation of the structural trilayer graphene was comprehensively regarded to the suggestion in the previous works to obtain an accuracy [50-51].

Figures 1a and 1b present the SEM images of nano-HOPG on a single crystal HOPG substrate. The schematic illustration of the square shape nano-HOPG arrayed on substrate cover area of $100 \times 100 \mu\text{m}^2$ are shown in Fig. 1c. We intend to create HOPG squares as small as possible in our work, and 300 nm is the smallest size achieved in our setup. We note that the array of nano-HOPG still remains single crystal according to the original substrate. Figure 1d shows the Fermi surface map of nano-HOPG which is circular (schematic red dash line) around the Brillouin zone (blue solid line). Although HOPG is azimuthally disordered of graphite, the band dispersion is invariant with azimuthal angles [52]. Figure 1e presents the valence band dispersion of HOPG measured along the black arrow shown in Fig. 1d. To observe band gap opening, we point out on the Dirac cone near the Fermi level (see the inset in Fig. 1e). Figure 2q exhibits the measurement position of ARPES spectra at 3 different areas: (i) nano-HOPG pattern (A); (ii) near nano-HOPG pattern (B); and (iii) HOPG substrate (C). As a result of the EDCs of valence band dispersion of nano-HOPG and HOPG substrate, as shown in Fig. 2r, there are different features at near Fermi level. A bandgap opening was found in the nano-HOPG pattern that was indicated by the EDC symmetrized ARPES spectrum, as seen in Fig. 1f.

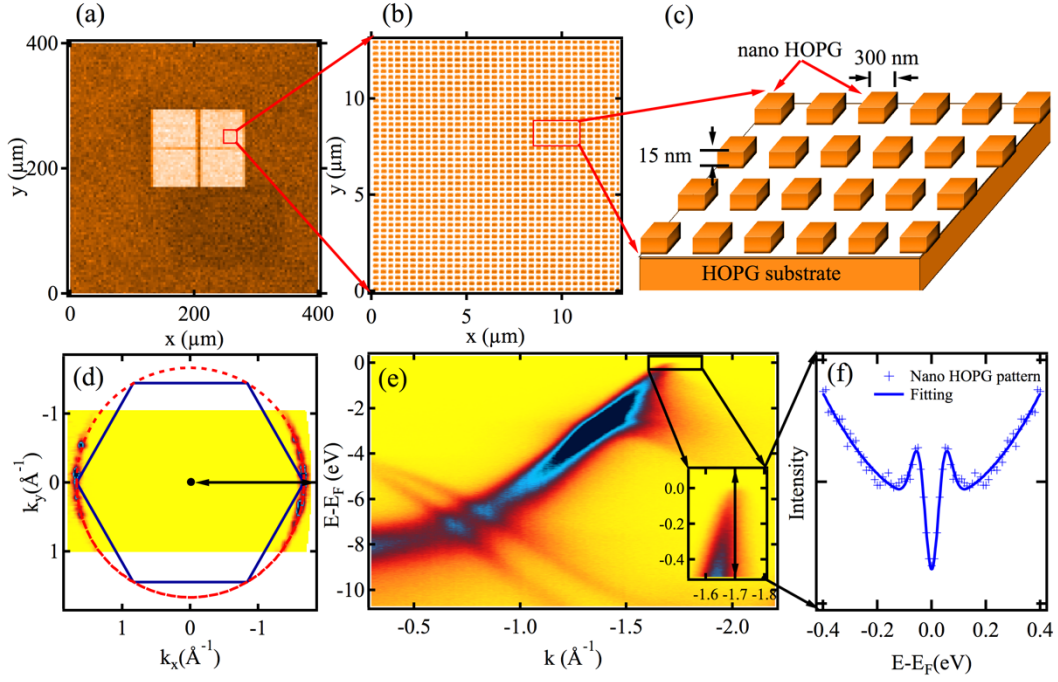


Fig. 1 (a) and (b) SEM image of nano-scale HOPG. (c) Schematic of nano-scale HOPG on HOPG substrate. Electronic structure of highly oriented pyrolytic graphite (HOPG) (measured by using 60 eV of photon energy) consist of (d) Fermi surface map of HOPG and (e) Band dispersion along black arrow in fig. (d). Inset fig. in (e) is band dispersion near Fermi level in black solid box. (f) Symmetrized EDC spectrum across k_F of nano-HOPG (measured by using 95 eV of photon energy).

Figure 2 presents electronic structure, which was taken by 95 eV of photon energy. Figures 2a – 2d show the band dispersion near the Fermi level of nano-HOPG, HOPG substrate, near nano-HOPG, and Au, respectively, which is correspond to the energy dispersion curve (EDC) spectra at k_F as shown in Figs. 2i - 2l. Normally, graphene or graphite has the Dirac cone at the K point of the Brillouin zone near the Fermi level. In the case of nano-HOPG, we find the density of state with an EDC peak at approximately 59 meV below Fermi level, suggesting that there is a gap opening in nano-HOPG. The bandgap opening in the nano HOPG pattern can be clearly observed in symmetrized ARPES spectra using Fermi level of Au as a reference for Fermi level.

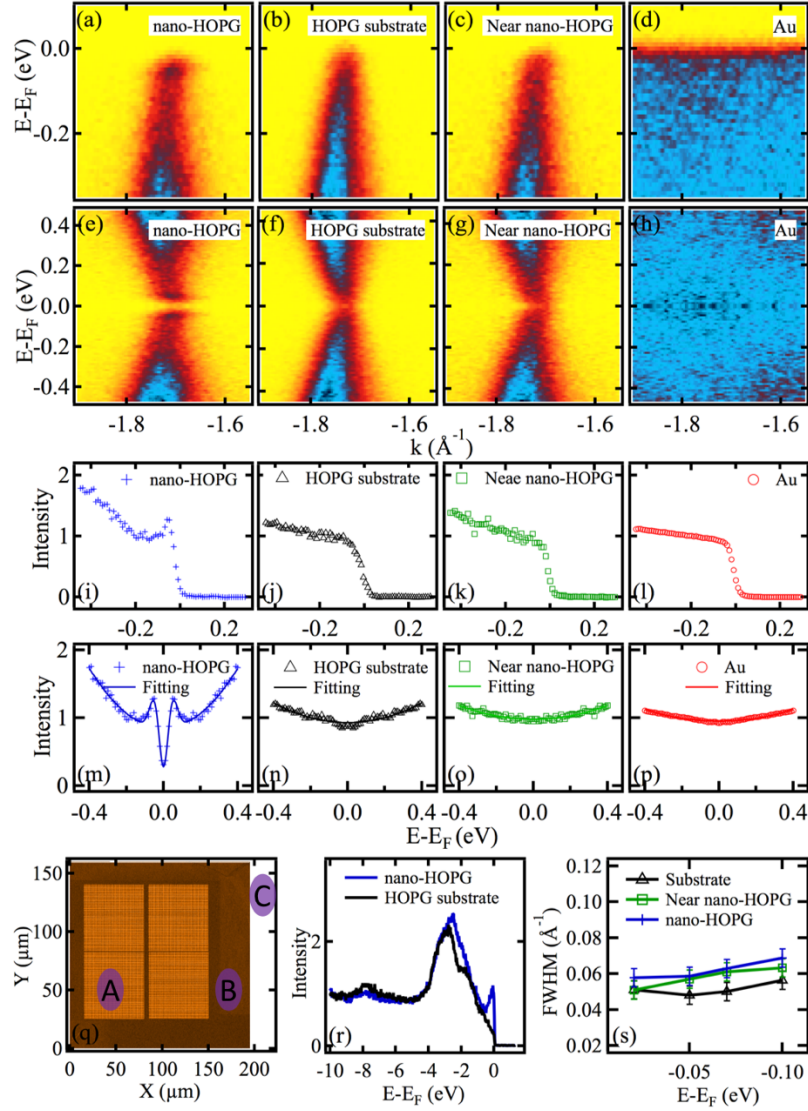


Fig. 2 The ARPES were measured by using 95 eV of photon energy. (a) – (d) ARPES spectra of nano HOPG pattern, HOPG substrate, near nano HOPG pattern, and gold at near Fermi level, respectively. (e) – (h) Symmetrized ARPES spectra of (a) – (d) respectively. (i) – (l) EDC spectra across k_F of ARPES spectra (a) – (d) respectively. (m)-(p) EDC spectra across k_F of symmetrized ARPES spectra (e) – (h). (q) ARPES measurement positions of nano HOPG pattern (A), near nano HOPG pattern (B) and HOPG substrate (C) that are far from the pattern by 1 mm. (r) EDC spectra across k_F of the valence band of the nano HOPG pattern and the HOPG substrate. (s) FWHM of MDC spectra of nano HOPG pattern, near nano HOPG pattern and HOPG substrate.

The symmetrized band dispersion near the Fermi level of nano-HOPG, HOPG substrate, near-nano HOPG, and Au are shown in Figs. 2e – 2h, respectively. The corresponding of EDC spectra of these symmetrized band dispersion near the Fermi level are shown in Figs. 2m – 2p. The energy bandgap of 112 ± 15 meV was observed on the symmetrized EDC spectrum of nano-HOPG (Fig. 2(m)). The curves shown in Figs. 2m-2p are guided by the eyes. The ARPES data of the nano-HOPG was measured at the beamline 5-4, Stanford Synchrotron Radiation Lightsource, in the USA for a reproducibility test, which shows a similar result. The bandgap opening was reproducibly observed in nano-HOPG shown in Fig. S2.

Regarding the origin of the bandgap opening, the quantum confinement effect is the first candidate to explain the bandgap opening because of the nano-scale of the sample. Normally, nano-sized graphite-based materials can be a semiconductor materials due to a bandgap caused by the quantum confinement effect. The shrinking of the bandgap depends on the size of the nanoparticle. This effect is dominant in the electronic structure of a few-nanometer particle [53]. In this work, the energy bandgap of the nano HOPG pattern is larger than other graphene-base nanoscale (GQD, GNR) at the same size, up to 1 order of magnitude [22]. Therefore, the quantum confinement effect is not the primary reason of the gap opening in our case.

We then tried to look for another cause of this bandgap opening. The twist angle of the top layer of nano HOPG was taken into consideration for bandgap opening because HOPG is azimuthally disordered. A flat band must fit into the gap left by the multilayer graphene's twist angle [1]. The flat band disappeared in our measurements when we found a bandgap on nano HOPG. We can therefore conclude that our gap was not brought on by the multilayer graphene's twist angle. Regarding to the studies of ion

beam effect on sample surface, the ion beam created edge of nano hole or nano island that was dominated by zigzag edge [54-55].

Moreover, the ion beam is the cause of the disordered structures (dominated by sp^3) that were observed by the Raman technique. The disorder structure depends on the density of ion dose, and the HOPG surface becomes amorphous at a high ion dose [56-57]. Additionally, the sp^3 defect can transform metallic into semiconducting in multilayer graphene [58]. Figure 3 shows the Raman spectra of the HOPG substrate, near nano-HOPG pattern, and nano-HOPG pattern. The disorder peak (D peak) of the nano HOPG pattern and near nano-HOPG pattern, shown in green and blue solid lines, reveals an ion beam sputtered disorder defect while the D peak is not present in the normal HOPG surface, shown in black solid line. We also extract the FWHM of the momentum distribution curve (MDC) to identify the disorder in ARPES data [59]. According to the MDCs fitting results as shown in Fig. 2s, the FWHMs of the nano HOPG pattern and near nano-HOPG pattern are also similar. Since the bandgap opening is only observed in the nano-HOPG pattern, we then rule out that the disorder is the main cause of the bandgap opening.

The next possibility that we consider the strain effect on nano-HOPG. The strain is an effect on the vibrational frequency of molecules, as indicated by a shift in the Raman frequency of the vibrational mode. C-C bound in G mode and 2D mode are in-plane vibrational modes. The frequencies of G mode and 2D mode are shifted to a higher frequency due to the compressive strain on the hexagonal carbon ring and oxygenation of graphite as observed in graphene oxide and graphite [60]. On the other hand, the frequencies of G mode and 2D mode are shifted to lower frequencies if there is tensile strain. Due to the broad spectra of G mode, 2D mode was used to be characterized. 2D mode of Raman spectrum was divided into two Lorentzian peaks

[61]. By Lorentzian fitting, the peak position of second peak of the nano-HOPG is significantly redshifted which is 4 cm^{-1} compared to the HOPG surface as shown in inset of Fig. 3. The redshift refers to a decrease in frequency of 2D mode which may confirm that the organic bonding is not dominated on nano-HOPG. Moreover, there is a possibility that this redshift may come from expansion of carbon hexagonal ring which is called tensile strain [62]. Additionally, strain has been reported in nanopatterned monolayer MoS_2 and modulates the photoluminescence [63]. As a result, it is suggested that a small amount of tensile strain may occur on nano-HOPG.

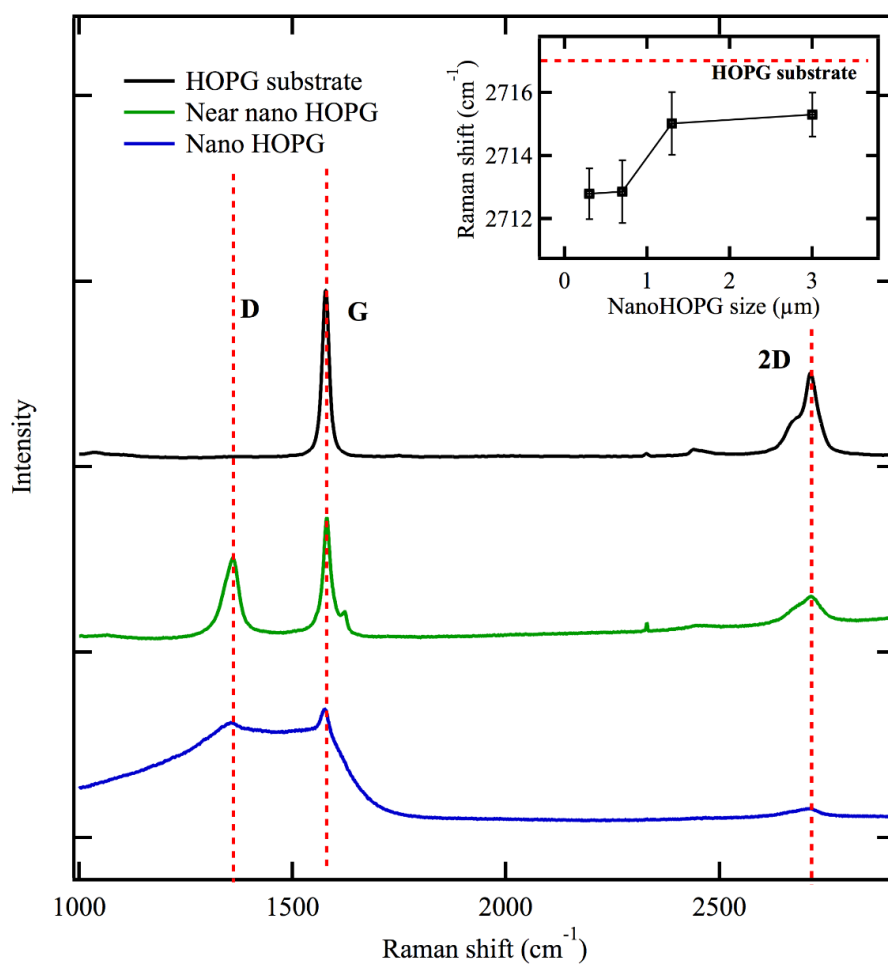


Fig. 3 Raman spectra of HOPG substrate, near nano-HOPG pattern and nano-HOPG pattern. The peak positions of the D band, G band, and 2D band were indicated by the

red dashed lines. The inset shows the fitting of peak positions of the 2D bands of each nano-HOPG size and HOPG substrate.

To obtain insight in the strain effect on the bandgap opening observed in nano-HOPG, we performed the electronic structure calculations under strain effect shown in Fig. 4. For illustrative purposes, the unit cell of the distorted and pristine HOPG are superimposed (Fig. 4a), implying the structural difference between a pristine and distorted case with AB stacking sequence. In this configuration, the second C sub-layer of the first layer (from top) contains distortion. To investigate the distortion dependence of HOPG electronic structure, one C atom is shifted close to the other along \vec{b} direction by distorted values $\Delta(\text{\AA}) \in [-0.155, -0.006]$ with step 0.025 \AA . Fig. 4b illustrates the selected band dispersion by compressing $\Delta(\text{\AA}) = [-0.155, -0.105, -0.006]$ and one case of stretching $\Delta(\text{\AA}) = 0.042$ along $\Gamma - K$, computed by one-step photoemission theory, of various HOPG configurations. The position of the Fermi level was rearranged for the DFT calculations to align the top of the calculated valance band with the one from ARPES measurements, namely adding 0.08 eV to the binding energy as an offset. The position of high-symmetry points differs to literature due to impacts of the incident angle of light. Clearly, highly dispersive bands are found along this direction. For instance, there is always the fact that one band possesses the top of dispersion at the Γ point and disperses toward the higher binding energy on approaching the K point. Deformation brings several trends regarding to distorting level. When $|\Delta|$ reduces from 0.155 \AA to 0.006 \AA , some top-most bands around Γ move down and overlay to others. In contrast, those bands surrounding Γ starts to split and go up as Δ reaches 0.042 \AA . Furthermore, the band in the vicinity of K is shifted to the right side. Noticeably, at the beginning the energy bandgap emerges, reduces and closes later on. Figs. 4c and 4d show the simulated stretched and raw-data experimental spectra of investigated

HOPGs. Calculated models take into consideration the experiment geometry and as many parameters as possible that were used in experiments. From computational point of view, stretching the topmost layer by 0.080 Å along \vec{b} direction creates a bandgap $E_g = 137$ meV meanwhile $E_g = 112$ meV is observed in ARPES measurements. In general, there is a good agreement between computational and measured data in terms of band-gap appearance and major dispersion features around high-symmetry points. Nevertheless, we notice a difference concerning the band-gap value. Partially the later discrepancy might be due to the low accuracy of our DFT exchange-correlation functional. Overestimation can happen when considered band gaps are smaller than 1 eV [64]. HOPG is well-known as a semimetallic material which is certified by many previous studies [65-67]. However, it can behave semiconducting by being irradiated by visible polarized light perpendicular to its planes [68]. By various techniques (e.g., scanning tunneling microscope (STM) or temperature-dependent resistance), energy gap of graphite is found in order of $\sim 30 - 40$ eV [69,70]. The best HOPG samples are supposed to own crystallites preferentially oriented in such a way that mosaic angle spread is less than one degree [71]. Consequently, electronic properties strongly depend on the alignment of graphite crystals along c-axis. Depending on how layers are stacked, HOPG is classified into either well-ordered structures (metallic) or poorly ordered ones (semiconducting) [72]. In addition, stacking fault defects are proposed to be a cause of anomalously high resistivity and quantum transport in HOPG [73,74]. Experimentally, horizontal shifts in the HOPG top layer, produced by a STM tip, lead to transitions between ABA and ABC stacking [75]. Therefore, not surprisingly our work indicates the semiconductor fingerprint and one potential trigger for the bandgap creation of HOPGs, which is in harmony with above-mentioned papers. Our introduced energy bandgap (137 meV and 112 meV) are greater than former reports [76-79]. It is

noteworthy that this inequality is likely from different scanned sample areas, energy resolution and not mentioned parameters in ARPES publications. To further confirm the bandgap opening at K point, we calculated the photon energy dependence of ARPES of the stretched configuration displayed in Fig. 4c. Energy distribution curves (EDCs) imply that constituting states are gaped within the photon energy range differently. Thus, our findings emphasize the confidence interpretation of a bandgap existing in HOPGs.

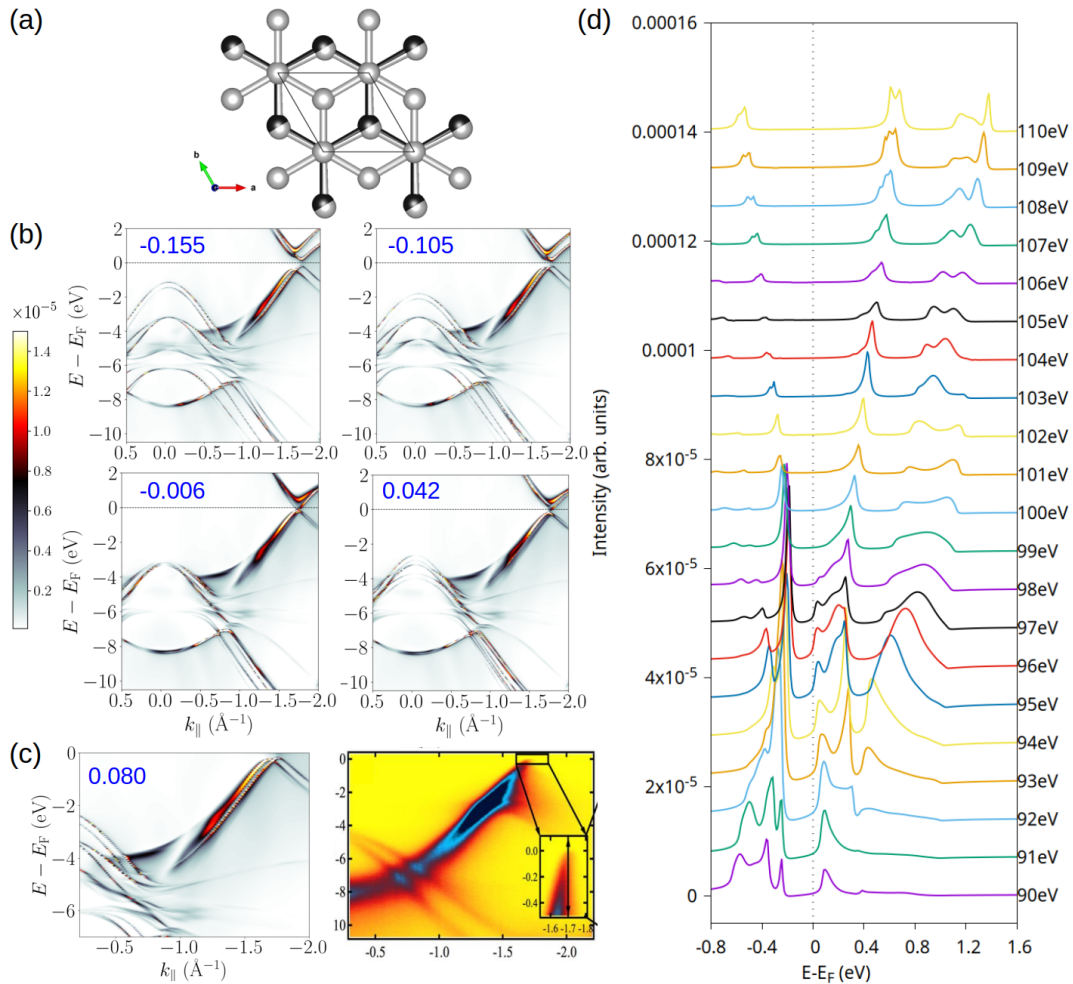


Fig. 4 Electronic band structure of bulk HOPG. (a) Top view of the distorted (gray, top) and pristine (black, bottom) HOPG unit cells, shown superimposed for illustrative

purposes. (b) ARPES intensity map calculated at a 95 eV photon energy along the $\bar{\Gamma} - \bar{K}$ line under selectively compressing (0.155, -0.105, -0.006) and stretching (0.042 Å) structures along (as illustrated in (a)). The blue labels indicate distorting values Δ . (c) Similar to (a) but with $\Delta = 0.080$ Å. (d) Energy distribution curve (EDC) computed at K point as a function of photon energy.

In addition to the above-mentioned multiple scattering method, we carried out the electronic band structure calculations by the pseudopotential method. Herein the investigation is applied a biaxial tensile strain. The relaxed structural unit cell of trilayer graphene was used for simulation multi-layer effect of graphene in HOPG, as shown in Fig. 5(a). In order to study band-gap opening, we considered the electronic band structure of trilayer graphene compared with monolayer graphene in the presence of biaxial tensile strain varying from 0 to 2% according to the schematic as shown in Fig. 5(b). From the experimental result, the Raman spectra of the 2D peak are shifted to lower frequency relating to the increase of the C-C bond length. In addition, the Raman 2D band corresponds with the iTO (A_1) phonon modes in D_{3h} symmetry, in which all carbon atoms on the carbon ring move towards and move outward the Γ -center. Therefore, the biaxial tensile is a possible type of strain that corresponds with 2D band vibration mode and plays an important role in expanding C-C bond length in all directions. The comparative energy gap as a function of biaxial tensile strain is depicted in Fig. 5(c). Note that the calculated energy gaps of graphene with applied strain are lower than the experimental values due to the common self-interaction error of DFT-PBE calculation [80]. The finding shows that the energy gap of monolayer graphene tends to linearly increase, whereas that of trilayer graphene is roughly increasing. The band structure of trilayer graphene in the absence of strain is shown in Fig. 5(e). During applied 0 to 2% strain, computational investigation reveals that the highest gap opening

of trilayer graphene is under 1.1% strain with an energy gap of 93.0 meV, which is close to the measured energy gap of HOPG (112 meV). Meanwhile, that of monolayer graphene is equal to 80.9 meV, which is lower. The corresponding band structure at K-point is illustrated in Figs. 5(d) and 5(f) for monolayer and trilayer graphene at 1.1% strain, respectively. According to this computational result, it suggests that the biaxial tensile strain of trilayer graphene is likely responsible for the gap opening of HOPG.

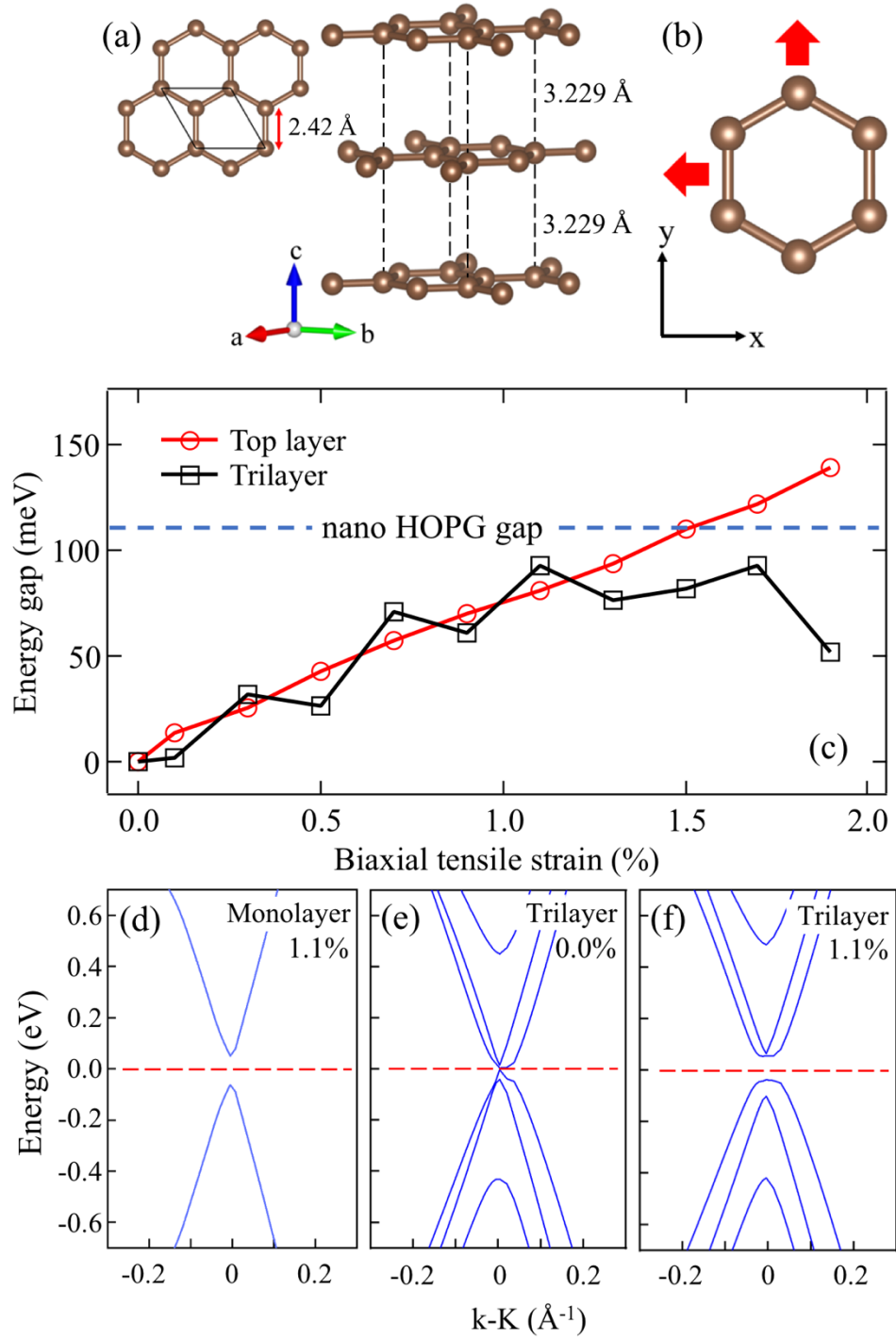


Fig. 5 (a) The geometric structure of trilayer graphene with corresponding C-C band distance and the interlayer spacing. (b) Schematic of biaxial tensile strain with a same strain value along x- and y-direction. (c) The comparative energy gap of monolayer, trilayer graphene, and nano HOPG. The corresponding band structure of monolayer

graphene with applied 1.1% strain (d), trilayer graphene with no strain (e), and trilayer graphene with applied 1.1% strain (f).

Moreover, we use the DFT calculation to study the energy band dispersion along k_z direction of the 1.1% biaxial tensile strain on three layers of graphene as shown in Fig. 6. We observed that the dispersion clearly shows no bandgap closing at all k points. From the ARPES data at different k_z (see Fig. S3) and the DFT calculations, it suggests to the observed bandgap opening through the Brillouin zone along k_z . Note that the same behavior along k_z is also observed in the similar system MoS₂ [81].

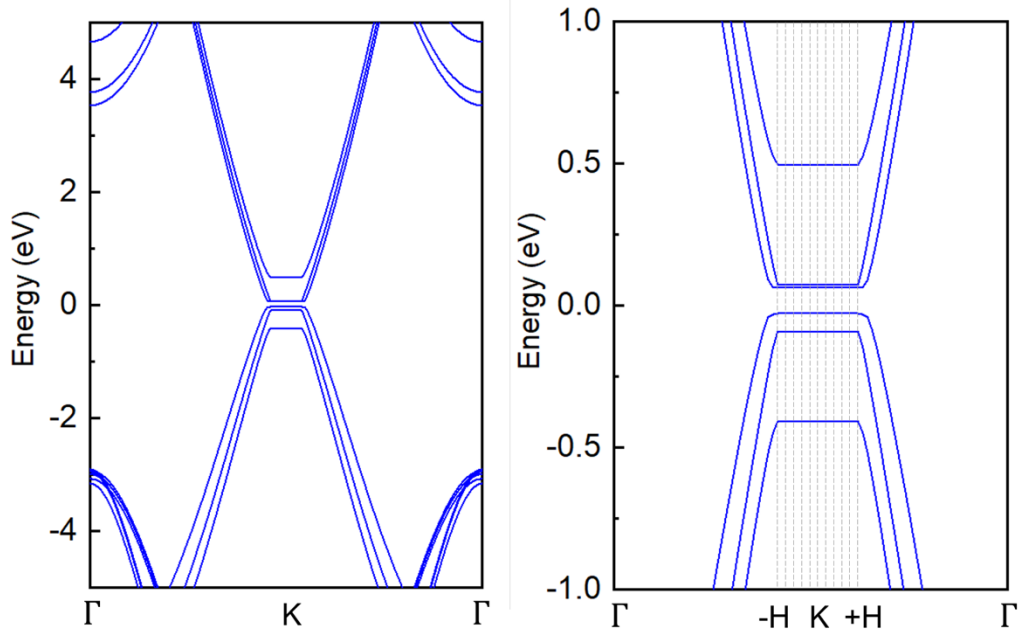


Fig. 6 Band structure of three layers graphene with 1.1 % of biaxial tensile strain.

We have shown the bandgap opening of nanoscale crystalline exists in the hundreds of meV range, which corresponds to the energy range from mid-infrared to terahertz. In comparison to previous research that found bandgaps in single crystal graphene, the bandgaps created by the various methods are identical in the hundreds of meV range. For example, an electric field generated in bilayer graphene [16,82], whereas graphene grown on a SiC substrate has a bandgap of 260 meV for a single

layer and decreases with the number of layers [15]. Additionally, it is effective when the tensile strain of graphene with a bandgap of 300 meV at 1% tensile strain is calculated, and the energy bandgap reduces as the number of layers rises with the same tensile strain [41]. As a result, the bandgap of nanoscale crystalline determined by theoretically and experimentally in this study is comparable to that of graphene crystalline determined in previous research investigations.

In summary, we show the energy bandgap opening in the order of 100 meV occurred at the surfaces of nano-scale HOPG square patterns by calculations from 2 different methods (full-potential scattering and pseudopotential in conjunction with variational principles), supporting the experiment ARPES observation. The Raman shift and DFT calculations suggest that tensile strain is likely the origin of this bandgap opening with two strained configurations. The semi-infinite crystal with 0.080 Å distortion in the top-most layer possesses an energy bandgap of 137 meV. The trilayer model under the biaxial tensile strain reveals the gap of 93 meV. The present study connects strain effects to photoemission and proposes solutions for band-gap engineering, which opens the door to several promising applications across tunable photodetectors and light-emitting devices. Our finding also demonstrates how to create a crystalline nanopattern whose energy bandgap is compatible with the terahertz application. We believe that our method will also provide a route to modify electronic structure of other crystalline materials/metasurfaces [83] which will be useful not only in the terahertz devices but also other optoelectronics.

Data availability

The authors declare that the main data supporting the findings of this study are available within the article and its Supplementary Information files.

Reference

- [1] Novoselov, K. S. et al. Electric field effect in atomically thin carbon films. *Science* **306**, 666-669 (2004).
- [2] Novoselov, K. S. et al. Two-dimensional gas of massless Dirac fermions in graphene. *Nature* **438**, 197-200 (2005).
- [3] Zhang, Y., Tan, Y. W., Stormer, H. L. & Kim P. Experimental observation of the quantum Hall effect and Berry's phase in graphene. *Nature* **438**, 201-204 (2005).
- [4] Li, Y., Tantiwanichapan, K., Sawan, A. K. & Paiella, R. Graphene plasmonic devices for terahertz optoelectronics. *Nanophotonics* **9**, 1901-1920 (2020).
- [5] Low, T. & Avouris, P. Graphene plasmonics for terahertz to mid-infrared applications. *ACS nano* **8**, 1086-1101 (2014).
- [6] Ju, L. et al. Graphene plasmonics for tunable terahertz metamaterials. *Nat. Nanotechnol.* **6**, 630-634 (2011).
- [7] Yan, H. et al. Tunable infrared plasmonic devices using graphene/insulator stacks. *Nat. nanotechnol.* **7**, 330-334 (2012).
- [8] Kim, B. S., Rhim, J. W., Kim, B., Kim, C. & Park, S. R. Determination of the band parameters of bulk 2H-MX₂ (M= Mo, W; X= S, Se) by angle-resolved photoemission spectroscopy. *Sci. Rep.* **6**, 1-7 (2016).
- [9] Winzer, T. Knorr, A. & Malic, E. Carrier multiplication in graphene. *Nano Lett.* **10**, 4839-4843 (2010).
- [10] Nair, R. R. et al. Fine structure constant defines visual transparency of graphene. *Science* **320**, 1308-1308 (2008).
- [11] Nguyen, T. D., Liu, S., Kumar, G., Nahata, A. & Vardeny, Z. V. Terahertz plasmonic properties of highly oriented pyrolytic graphite. *Appl. Phys. Lett.* **102**, 171107 (2013).

- [12] Yan, H. et al. Tunable infrared plasmonic devices using graphene/insulator stacks. *Nat. nanotechnol.* **7**, 330-334 (2012).
- [13] Gayduchenko, I. et al. Tunnel field-effect transistors for sensitive terahertz detection *Nat. Commun.* **12**, 1-8 (2021).
- [14] Li, P., Zhao, C. Y., Alu, A. & Yu, E. T. Experimental realization and modeling of a subwavelength frequency-selective plasmonic metasurface *Appl Phys Lett.* **99**, 221106 (2011).
- [15] Zhou, S. Y. et al. Substrate-induced bandgap opening in epitaxial graphene. *Nat. Mater.* **6**, 770-775 (2007).
- [16] Ohta, T., Bostwick, A., Seyller, T., Horn, K. & Rotenberg, E. Controlling the electronic structure of bilayer graphene. *Science* **313**, 951-954 (2006).
- [17] Sutter, P., Sadowski, T. J., & Sutter, E. Graphene on Pt (111): Growth and substrate interaction. *Phys. Rev. B* **80**, 245411 (2009).
- [18] Avila, J. et al. Exploring electronic structure of one-atom thick polycrystalline graphene films: A nano angle resolved photoemission study. *Sci. Rep.* **3**, 1-8 (2013).
- [19] Sprinkle, M. et al. First direct observation of a nearly ideal graphene band structure. *Phys. Rev. Lett.* **103**, 226803 (2009).
- [20] Knox, K. R. et al. Spectromicroscopy of single and multilayer graphene supported by a weakly interacting substrate. *Phys. Rev. B* **78**, 201408 (2008).
- [21] Leem, C. S. et al. High-resolution angle-resolved photoemission studies of quasiparticle dynamics in graphite. *Phys. Rev. B* **79**, 125438 (2009).
- [22] Ritter, K. A. & Lyding, L. W. The influence of edge structure on the electronic properties of graphene quantum dots and nanoribbons. *Nat. Mater.* **8**, 235-242 (2009).

- [23] Ebert, H., Ködderitzsch, D. & Minár, J. Calculating condensed matter properties using the KKR-Green's function method—recent developments and applications. *Rep. Prog. Phys.* **74**, 096501, (2011).
- [24] Ebert, H. The Munich SPR-KKR package, version 8.6. <https://www.ebert.cup.uni-muenchen.de/index.php/en/software-en/13-sprkkkr> (2021).
- [25] Wyckoff, R. W. G. Second edition. Interscience Publishers, New York, New York *Crystal Structures* **1**, 7-83. (1963).
- [26] Lloyd, P. Wave propagation through an assembly of spheres: II. The density of single-particle eigenstates. *Proc. Phys. Soc.* **90**, 207, (1967).
- [27] Pendry, J. B. Low-energy electron diffraction. In *Interaction of Atoms and Molecules with Solid Surfaces*, Boston, MA: Springer US., pp. 201-211, (1974).
- [28] Pendry, J. B. Theory of photoemission. *Surf. Sci.* **57**, 679-705, (1976).
- [29] Hopkinson, J. F. L., Pendry, J. B., & Titterton, D. J. Calculation of photoemission spectra for surfaces of solids. *Comput. Phys. Commun.* **19**, 69-92, (1980).
- [30] Beaulieu, S. et al. Revealing hidden orbital pseudospin texture with time-reversal dichroism in photoelectron angular distributions. *Phys. Rev. Lett.* **125**, 216404. (2020).
- [31] Rienks, E. D. et al. Large magnetic gap at the Dirac point in Bi₂Te₃/MnBi₂Te₄ heterostructures. *Nature* **576**, 423-428, (2019).
- [32] Krempaský, J. et al. Entanglement and manipulation of the magnetic and spin-orbit order in multiferroic Rashba semiconductors. *Nat. Commun.* **7**, 13071. (2016).
- [33] Gray, A. X. et al. Bulk electronic structure of the dilute magnetic semiconductor Ga_{1-x}Mn_xAs through hard X-ray angle-resolved photoemission. *Nat. Mater.* **11**, 957-962 (2012).
- [34] Strocov, V. N. et al. High-energy photoemission final states beyond the free-electron approximation. *Nat. Commun.* **14**, 4827 (2023).

- [35] Braun, J., Minár, J. & Ebert, H. Correlation, temperature and disorder: Recent developments in the one-step description of angle-resolved photoemission. *Phys. Rep.*, **740**, (2018).
- [36] Minár, J., Braun, J., Mankovsky, S. & Ebert, H. Calculation of angle-resolved photo emission spectra within the one-step model of photo emission—Recent developments. *J. Electron Spectros. Relat. Phenomena* **184**, 91-99 (2011).
- [37] Venturini, F., Minár, J., Braun, J., Ebert, H. & Brookes, N. B. Soft x-ray angle-resolved photoemission spectroscopy on Ag (001): Band mapping, photon momentum effects, and circular dichroism. *Phys. Rev. B* **77**, 045126 (2008).
- [38] Derondeau, G. et al. Fermi surface and effective masses in photoemission response of the $(\text{Ba}_{1-x}\text{K}_x)\text{Fe}_2\text{As}_2$ superconductor. *Sci. Rep* **7**, 1-8 (2017).
- [39] Krempaský, J., et al. Altermagnetic lifting of Kramers spin degeneracy. *Nature* **626**, 517-522. (2024).
- [40] Vo, T. P. et al. Analyzing core level photoelectrons by diffraction and circular dichroism via means of first-principle scattering calculations. *AIP Conf. Proc.* 3251, (2024).
- [41] Tkach, O. et al. Circular dichroism in hard X-ray photoelectron diffraction observed by time-of-flight momentum microscopy. *Ultramicroscopy* **250**, 113750 (2023).
- [42] Fedchenko, O. et al. Magnetic circular dichroism in core-level x-ray photoelectron spectroscopy of altermagnetic RuO_2 . [Manuscript in preparation].
- [43] Vo, T. P. et al. Layered Multiple Scattering Approach to Hard X-ray Photoelectron Diffraction: Theory and Application. *arXiv:2411.09669* (2024).
- [44] Kresse, G. & Furthmüller, J. Efficient iterative schemes for ab initio total-energy calculations using a plane-wave basis set. *Phys. Rev. B* **54**, 11169 (1996).

- [45] Kresse, G. & Furthmüller, J. Efficiency of ab-initio total energy calculations for metals and semiconductors using a plane-wave basis set. *Comput. Mater. Sci.* **6**, 15-50 (1996)
- [46] Perdew, J. P., Burke, K. & Ernzerhof, M. Generalized gradient approximation made simple. *Phys. Rev. Lett.* **77**, 3865 (1996)
- [47] Blöchl, P. E. Projector augmented-wave method. *Phys. Rev. B* **50**, 17953 (1994).
- [48] Grimme, S., Ehrlich, S. & Goerigk, L. Effect of the damping function in dispersion corrected density functional theory. *J. Comput. Chem.* **32**, 1456-1465 (2011)
- [49] Monkhorst, H. J. & Pack, J. D. Special points for Brillouin-zone integrations. *Phys. Rev. B* **13**, 5188 (1976).
- [50] Karasiev, V. V. et al. Communication: Simple and accurate uniform electron gas correlation energy for the full range of densities. *J. Chem. Phys.* **145**, 157101 (2016).
- [51] Gui, G., Li, J. & Zhong, J. Band structure engineering of graphene by strain: First-principles calculations. *Phys. Rev. B* **80**, 167402 (2009).
- [52] Zhou, S. Y. et al. Coexistence of sharp quasiparticle dispersions and disorder features in graphite. *Phys. Rev. B* **71**, 161403 (2005).
- [53] Kim, S. et al. Anomalous behaviors of visible luminescence from graphene quantum dots: interplay between size and shape. *ACS nano* **6**, 8203-8208 (2012).
- [54] Girit, C. O. et al. Graphene at the edge: stability and dynamics. *Science* **323**, 1705-1708 (2009).
- [55] Krauss, B. et al. Raman scattering at pure graphene zigzag edges. *Nano Lett.* **10**, 4544-4548 (2010).
- [56] Archanjo, B. S. et al. Ion beam nanopatterning and micro-Raman spectroscopy analysis on HOPG for testing FIB performances. *Ultramicroscopy* **111**, 1338-1342 (2011).

- [57] Rodriguez, R. D. et al. Ion-Induced Defects in Graphite: A Combined Kelvin Probe and Raman Microscopy Investigation. *Phys. Stat. Sol. (a)* **216**, 1900055 (2019).
- [58] Thiyagarajan, K., Ananth, A., Saravanakumar, B., Mok, Y. S. & Kim, S. J. Defect-induced metallic-to-semiconducting transition in multilayer graphene. *RSC Adv.* **5**, 16821-16827 (2015).
- [59] Hashimoto, M. et al. Effects of out-of-plane disorder on the nodal quasiparticle and superconducting gap in single-layer $\text{Bi}_2\text{Sr}_{1.6}\text{L}_{0.4}\text{CuO}_{6+\delta}$ (L= La, Nd, Gd). *Phys. Rev. B* **79**, 144517 (2009).
- [60] Perumbilavil, S., Sankar, P., Rose, T. P. & Philip, R. White light Z-scan measurements of ultrafast optical nonlinearity in reduced graphene oxide nanosheets in the 400–700 nm region. *Appl. Phys. Lett.* **107**, 051104 (2015).
- [61] Ferrari, A. C. et al. Raman spectrum of graphene and graphene layers. *Phys. Rev. Lett.* **97**, 187401 (2006).
- [62] Ni, Z. H. et al. Uniaxial strain on graphene: Raman spectroscopy study and band-gap opening. *ACS nano* **2**, 2301-2305 (2008).
- [63] Han, G. G. D. et al. Photoluminescent arrays of nanopatterned monolayer MoS_2 . *Adv. Funct. Mater.* **27**, 1703688. (2017).
- [64] Borlido, P. et al. Exchange-correlation functionals for band gaps of solids: benchmark reparametrization and machine learning. *Npj Comput. Mater.*, **6**, 1-17 (2020).
- [65] Zhou, S. Y., Gweon, G. H. & Lanzara, A. Low energy excitations in graphite: the role of dimensionality and lattice defects. *Ann. Phys.*, **321**, 1730-1746 (2006).
- [66] Cline, K. K., McDermott, M. T. & McCreery, R. L. Anomalously slow electron transfer at ordered graphite electrodes: influence of electronic factors and reactive sites. *J. Phys. Chem.*, **98**, 5314-5319 (1994).

- [67] Ye, T. et al. Mechanism and modulation of terahertz generation from a semimetal-graphite. *Sci. Rep.* **6**, 1-6 (2016).
- [68] Jellison Jr, G. E., Hunn, J. D. & Lee, H. N. Measurement of optical functions of highly oriented pyrolytic graphite in the visible. *Phys. Rev. B*, **76**, 085125 (2007).
- [69] Breusing, M., Ropers, C. & Elsaesser, T. Ultrafast carrier dynamics in graphite. *Phys. Rev. Lett.*, **102**, 086809 (2009).
- [70] García, N., Esquinazi, P., Barzola-Quiquia, J. & Dusari, S. Evidence for semiconducting behavior with a narrow band gap of Bernal graphite. *New J. Phys.*, **14**, 053015 (2012).
- [71] Zhamu, A. & Jang, B. Z. U.S. Patent No. 10,822,725. Washington, DC: U.S. Patent and Trademark Office (2020).
- [72] Pantin, V. et al. Electronic properties of high oriented pyrolytic graphite: Recent discoveries. *J. Phys. Chem. Solids*, **67**, 546-551 (2006).
- [73] Ono, S. et al. C-axis resistivity of graphite in connection with stacking faults *J. Phys. Soc. Jpn*, **40**, 498-504 (1976).
- [74] Arovas, D. P. & Guinea, F. Stacking faults, bound states, and quantum Hall plateaus in crystalline graphite. *Phys. Rev. B*, **78**, 245416 (2008).
- [75] Xu, P. et al. A pathway between Bernal and rhombohedral stacked graphene layers with scanning tunneling microscopy. *Appl. Phys. Lett.* **100**, 201601 (2012).
- [76] Leem, C. S. et al. Effect of linear density of states on the quasiparticle dynamics and small electron-phonon coupling in graphite” *Phys. Rev. Lett.* **100**, 016802 (2008).
- [77] Zhou, S. Y. et al. First direct observation of Dirac fermions in graphite. *Nat. Phys.* **2**, 595-599 (2006).
- [78] Grüneis, A. et al. Electron-electron correlation in graphite: a combined angle-resolved photoemission and first-principles study. *Phys. Rev. Lett.* **100**, 037601 (2008).

- [79] Sugawara, K., Sato, T., Souma, S., Takahashi, T. & Suematsu, H. Anomalous quasiparticle lifetime and strong electron-phonon coupling in graphite. *Phys. Rev. Lett.* **98**, 036801 (2007).
- [80] Mori-Sánchez, P., Cohen, A. J. & Yang, W. Localization and delocalization errors in density functional theory and implications for band-gap prediction. *Phys. Rev. Lett.* **100**, 146401 (2008).
- [81]. Kim, B. S., Rhim, J. W., Kim, B., Kim, C. & Park, S. R. Determination of the band parameters of bulk 2H-MX₂ (M= Mo, W; X= S, Se) by angle-resolved photoemission spectroscopy. *Sci. Rep.* **6**, 1-7 (2016).
- [82] Zhang, Y. et al. Direct observation of a widely tunable bandgap in bilayer graphene. *Nature* **459**, 820-823 (2009).
- [83] Deinert, J.-C. et al. Grating-graphene metamaterial as a platform for terahertz nonlinear photonics. *ACS nano* **15**, 1145-1154 (2020).

Acknowledgments

This work was supported by the Program Management Unit for Human Resources and Institutional Development, Research and Innovation (Thailand), Grant No. B39G670018, Suranaree University of Technology, Thailand Science Research and Innovation (TSRI) and National Science Research and Innovation Fund (NSRF). S.C. acknowledges DPST for financial support. This work was also supported by the project Quantum materials for applications in sustainable technologies (QM4ST), funded as project No. CZ.02.01.01/00/22 008/0004572 by Programme Johannes Amos Comenius, call Excellent Research (T.-P.V., J.M.) and the Czech Science Foundation Grant No. GA ĀR 23-04746S (T.-P.V.). The ARPES measurements are supported by beamline 09U1 of the Shanghai Synchrotron Radiation Facility, the CASSIOPEE

beamline, SOLEIL synchrotron, and beamline 5-2, Stanford Synchrotron Radiation Lightsource. We would also like to thank T. Taychatanapat, W. Saengsui, P. Laohana, A. Mooltang, S. Musikajareon, P. Chanprakhon, S. Polin and A. Rasritat for useful discussion and help with measurements.

Authors' Contributions

ARPES measurements were carried out by W.M., S.C., T.E., W.J., and C.J. W.M., S.C. and T.E. analyzed the ARPES data. HOPG sample came from H. N., and S.C. prepared nano scale crystalline HOPG samples. P.L.F., F.B., D.L. and Y.H. maintained the synchrotron photoemission endstation. One-step model calculations were performed by T.-P.V. and J.M. VASP calculations were done by I.F., S.S., W.L. and S.C. The manuscript was suggestions and comments by W.M., W.L. and I.F. W.M. conceived and designed the research and is responsible for overall project direction, planning and infrastructure.

Supplementary Information

See the Supporting Information for detail on symmetrized EDC spectra across k_F of each position of ARPES measurements in the $300 \times 300 \mu\text{m}^2$ array with a step size of $100 \mu\text{m}$ in x and y directions (i.e., 3×3 grid) and Reproduced of ARPES measurements at Stanford Synchrotron Radiation Lightsource, beamline 5-4. Moreover, we include the data of the observation of gap opening by using different photon energies (i.e., at different k_z) and a DFT calculation of the band along the k_z direction of the 1.1% biaxial tensile strain on three layers of graphene.

Supplementary Information for

Emergence of a Bandgap in Nano-scale Graphite: A Computational and Experimental Study

Sujinda Chaiyachad¹, Trung-Phuc Vo^{2,3}, Sirisak Singesen¹, Tanachat Eknapakul^{1,4},

Warakorn Jindata¹, Chutchawan Jaisuk¹, Patrick Le Fevre⁵, Francois Bertran⁵,

Donghui Lu⁶, Yaobo Huang⁷, Hideki Nakajima⁸, Watchara Liewrian⁹, Ittipon

Fongkaew¹, Ján Minár^{2,*} and Worawat Meevasana^{1,*}

¹School of Physics and Center of Excellence on Advanced Functional Materials,
Suranaree University of Technology, Nakhon Ratchasima 30000, Thailand

²New Technologies-Research Center, University of West Bohemia, 30100, Pilsen,
Czech Republic

³Institute of Physics, Czech Academy of Sciences, Cukrovarnická 10, 16200 Praha 6,
Czech Republic

⁴Functional Materials and Nanotechnology Center of Excellence, School of Science,
Walailak University, Nakhon Si Thammarat, 80160, Thailand

⁵Synchrotron SOLEIL, L'Orme des Merisiers, Départementale 128, F-91190 Saint-
Aubin, France

⁶Stanford Synchrotron Radiation Lightsource, SLAC National Accelerator Laboratory,
2575 Sand Hill Road, Menlo Park, California 94025, USA

⁷Shanghai Advanced Research Institute, Chinese Academy of Sciences No.99 Haik
Road, Zhangjiang Hi-Tech Park, Pudong Shanghai, P R China

⁸Synchrotron Light Research Institute, Nakhon Ratchasima 30000, Thailand

⁹Department of Physics, King Mongkut's University of Technology Thonburi,
Bangkok 10140, Thailand

E-mail: worawat@g.sut.ac.th and jminar@ntc.zcu.cz

Figure S1 shows the symmetrized EDC of ARPES spectra across k_F of HOPG surface that were performed at beamline 09U1 of the Shanghai Synchrotron Radiation Facility, China. This ARPES data were measured by using 95 eV of photon energy. This figure clarifies where the nano HOPG is located in the experiment section. Each position of ARPES measurements in the $300 \times 300 \mu\text{m}^2$ array with a step size of $100 \mu\text{m}$ in x and y directions (i.e., 3×3 grid). The nano-HOPGs are located at positions (i), (ii), and (iv).

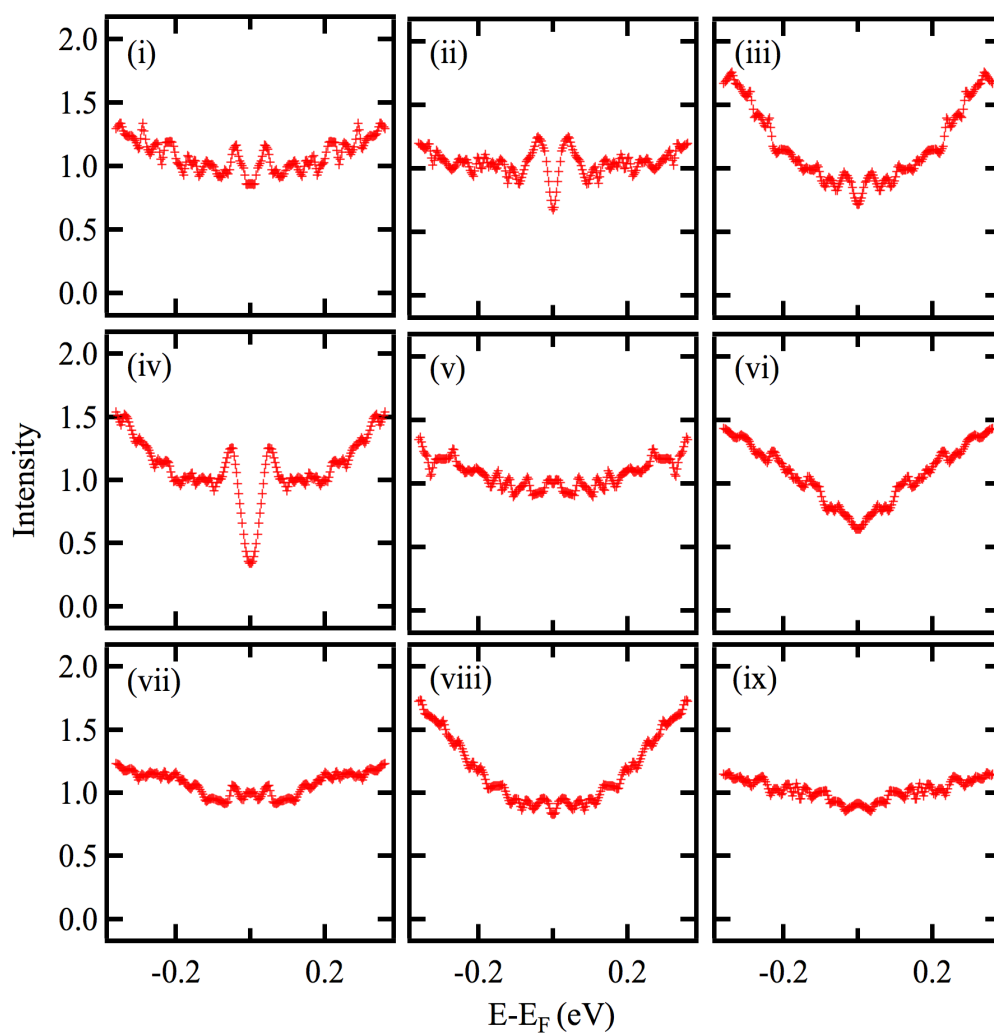


Fig. S1 (i)-(ix) Symmetrized EDC spectra across k_F of each position of ARPES measurements in the $300 \times 300 \mu\text{m}^2$ array with a step size of $100 \mu\text{m}$ in x and y directions (i.e., 3×3 grid).

Figure S2 illustrate the symmetrized EDC of ARPES spectra across k_F of nano-HOPG(i), HOPG surface(ii), and Au(iii). This data was measured by using 60 eV of photon energy at the beamline 5-4, Stanford Synchrotron Radiation Lightsource, in the USA.

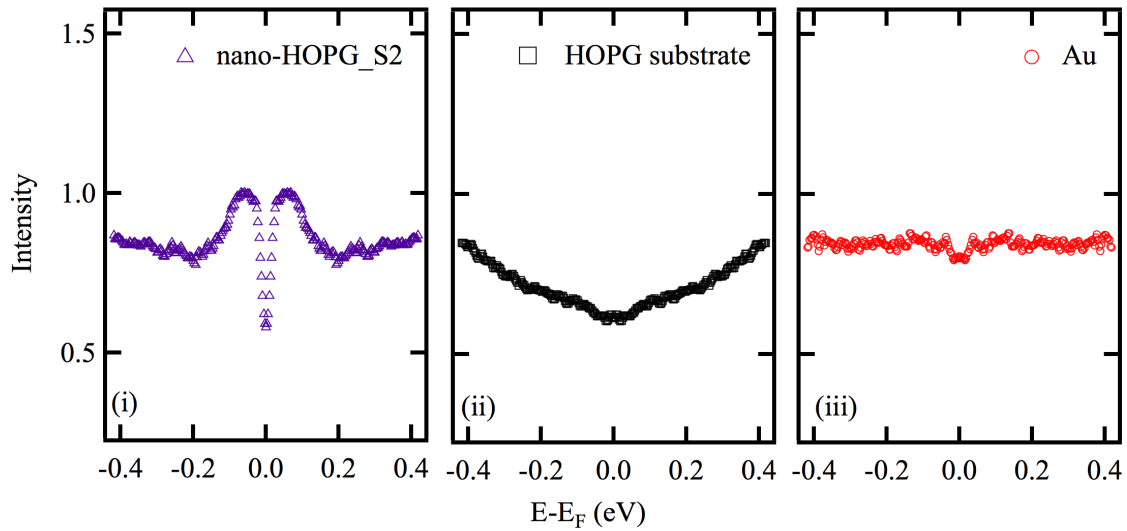


Fig. S2 ARPES measurements at Stanford Synchrotron Radiation Lightsource, beamline 5-4, (i)-(iii) symmetrized EDC spectra across k_F of ARPES spectra of nano-HOPG, HOPG substrate, and Au respectively.

From the ARPES measurement, we have observed the gap opening using different photon energies (i.e., at different k_z) as shown in Fig. S3 below 60 eV (Figs. S3a–S3d) and 95 eV (Figs. S3e–S3h).

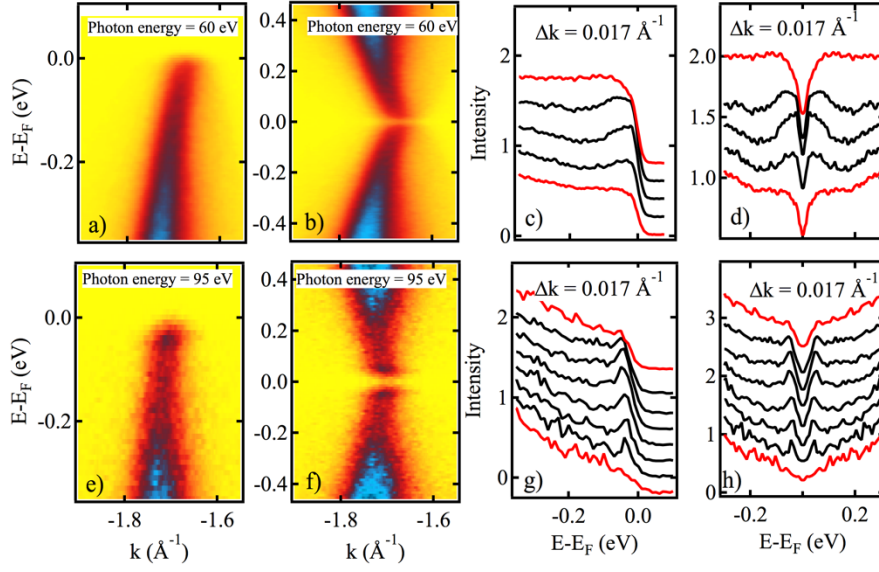


Fig. S3 ARPES spectra of nano HOPG that was measured at 60 eV (a) and 95 eV (e). The symmetrized ARPES spectra of (a) and (e) are shown in (b) and (f), respectively. EDC spectra near k_F of (a) and (e) in (c) and (g), respectively. EDC spectra near k_F of (b) and (f) are shown in (d) and (h), respectively.